Cell Reports

Interstitial Migration of CD8αβ T Cells in the Small Intestine Is Dynamic and Is Dictated by Environmental Cues

Graphical Abstract

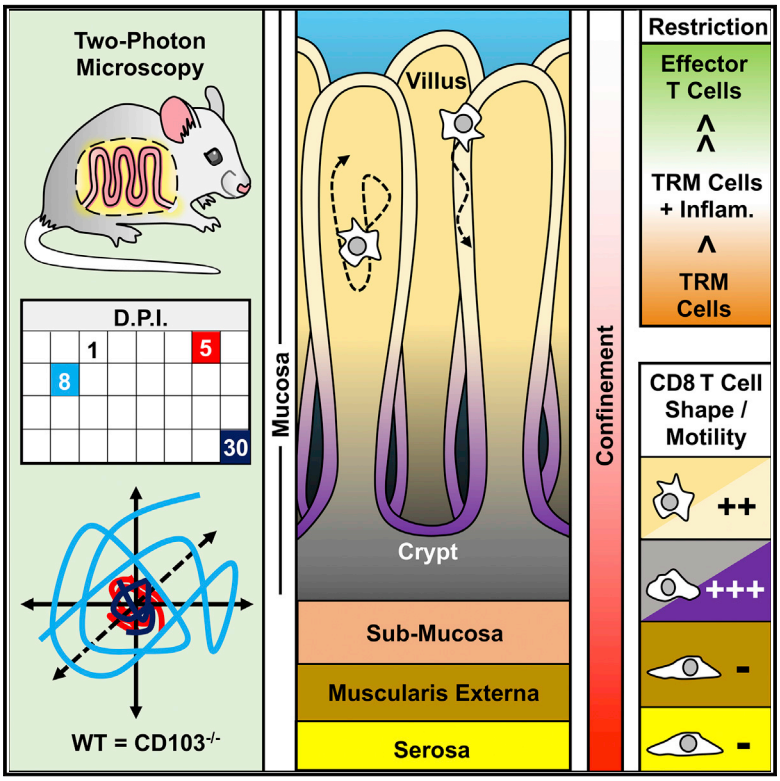

Highlights

- CD8 T cell movement in the small intestine is constrained by architecture
- Antiviral CD8 T cell motility is dynamic and changes throughout infection
- Motility is restricted during memory responses and is CD103 independent
- Self-specific CD8 T cells initially arrested with antigen, but accelerate when tolerant

Authors

Emily A. Thompson, Jason S. Mitchell, Lalit K. Beura, ..., David Masopust, Brian T. Fife, Vaiva Vezys

Correspondence

vvezys@umn.edu

In Brief

Using *in vivo* imaging of pathogen- and self-specific CD8 T cells in the small intestine, Thompson et al. reveal dynamic changes in the speed and volume of tissue surveyed by CD8 T cells over time after antigen encounter. Migration was CD103 independent, and motility was most limited during the memory response.

Thompson et al., 2019, Cell Reports *26*, 2859–2867
March 12, 2019
https://doi.org/10.1016/j.celrep.2019.02.034

CellPress

Cell Reports
Report

Interstitial Migration of CD8αβ T Cells in the Small Intestine Is Dynamic and Is Dictated by Environmental Cues

Emily A. Thompson,[1,2] Jason S. Mitchell,[2,3] Lalit K. Beura,[1,2] David J. Torres,[5] Paulus Mrass,[6] Mark J. Pierson,[2,3] Judy L. Cannon,[6] David Masopust,[1,2] Brian T. Fife,[2,4] and Vaiva Vezys[1,2,7,*]
[1]Department of Microbiology and Immunology, University of Minnesota, Minneapolis, MN 55455, USA
[2]Center for Immunology, University of Minnesota, Minneapolis, MN 55455, USA
[3]Department of Laboratory Medicine and Pathology, University of Minnesota, Minneapolis, MN 55455, USA
[4]Department of Medicine, University of Minnesota, Minneapolis, MN 55455, USA
[5]Department of Mathematics and Physical Science, Northern New Mexico College, Espanola, NM 87532, USA
[6]Department of Molecular Genetics and Microbiology, University of New Mexico, Albuquerque, NM 87131, USA
[7]Lead Contact
*Correspondence: vvezys@umn.edu
https://doi.org/10.1016/j.celrep.2019.02.034

SUMMARY

The migratory capacity of adaptive CD8αβ T cells dictates their ability to locate target cells and exert cytotoxicity, which is the basis of immune surveillance for the containment of microbes and disease. The small intestine (SI) is the largest mucosal surface and is a primary site of pathogen entrance. Using two-photon laser scanning microscopy, we found that motility of antigen (Ag)-specific CD8αβ T cells in the SI is dynamic and varies with the environmental milieu. Pathogen-specific CD8αβ T cell movement differed throughout infection, becoming locally confined at memory. Motility was not dependent on CD103 but was influenced by micro-anatomical locations within the SI and by inflammation. CD8 T cells responding to self-protein were initially affected by the presence of self-Ag, but this was altered after complete tolerance induction. These studies identify multiple factors that affect CD8αβ T cell movement in the intestinal mucosa and show the adaptability of CD8αβ T cell motility.

INTRODUCTION

The small intestine (SI) is the largest mucosal interface between the host and the outside environment and is the entry site for many microbes, which can quickly disseminate throughout the body. Therefore, evaluating immune cell surveillance in this compartment is of great interest. Many elegant studies have assessed the motility of unconventional and CD4 T cells in the SI, but the migratory behavior of adaptive CD8αβ T cells in this tissue is unknown (Edelblum et al., 2012; Hoytema van Konijnenburg et al., 2017; Sujino et al., 2016; Sumida et al., 2017; Wang et al., 2014; Xu et al., 2012). After systemic lymphocytic choriomeningitis virus (LCMV) infection that broadly positions CD8 T cells throughout the mouse, there are only six antigen (Ag)-specific CD8 resident memory T cells (T_{RM}) found per every 1,000 nucleated cells in the SI at a memory time point (Steinert et al., 2015). This, combined with the distinctive sub-anatomical features of the SI, create a unique challenge for adequate patrolling of this tissue by CD8 T cells.

Using two-photon laser scanning microscopy (TPLSM), we show that CD8 T cell motility in the SI jejunum is dynamic and largely dependent on context, such as the stage of infection and inflammatory milieu. Furthermore, the physical location of CD8 T cells within anatomical compartments of the SI dictated their migratory behavior. Dissecting the motile behavior of CD8 T cells during the steady state and infection has broadened our knowledge of effective CD8 T cell immune surveillance in the SI and informs the development of vaccines and treatments targeting pathogens or malignancies requiring CD8 T cell responses.

RESULTS

Ag-Specific CD8αβ T Cell Motility in the SI Is Dynamic during Infection

To assess the motile behavior of CD8 T cells during infection, naive P14-GFP CD8 T cells, which recognize the gp33 epitope of LCMV, were transferred to B6 mice that were subsequently infected with LCMV (Figure S1A). At days 5, 8, and 30 after LCMV infection, P14-GFP CD8 T cells were detected in both the epithelium and lamina propria (LP) of the SI using flow cytometry (Figure S1B). At all time points, P14-GFP CD8 T cells in the villi of explanted jejunum were motile in three dimensions (Figures 1A and S1C; Videos S1 and S2). While P14-GFP CD8 intraepithelial lymphocytes (IEL) continuously probed the tissue, P14-GFP CD8 LP lymphocytes (LPL) exhibited a smooth, gliding motion along other cells (Videos S1 and S2). We observed P14 CD8 T cells moving between the epithelium and the LP, which has been seen with γδ T cells (Sujino et al., 2016). Ag-specific P14-GFP CD8 T cells were never observed "space walking" (i.e., traversing the lumen between villi). Occasionally, CD8 T cells traveled from villus to villus through the LP at the base of the villi near the crypt-villi junctions (data not shown). Villi tilting during

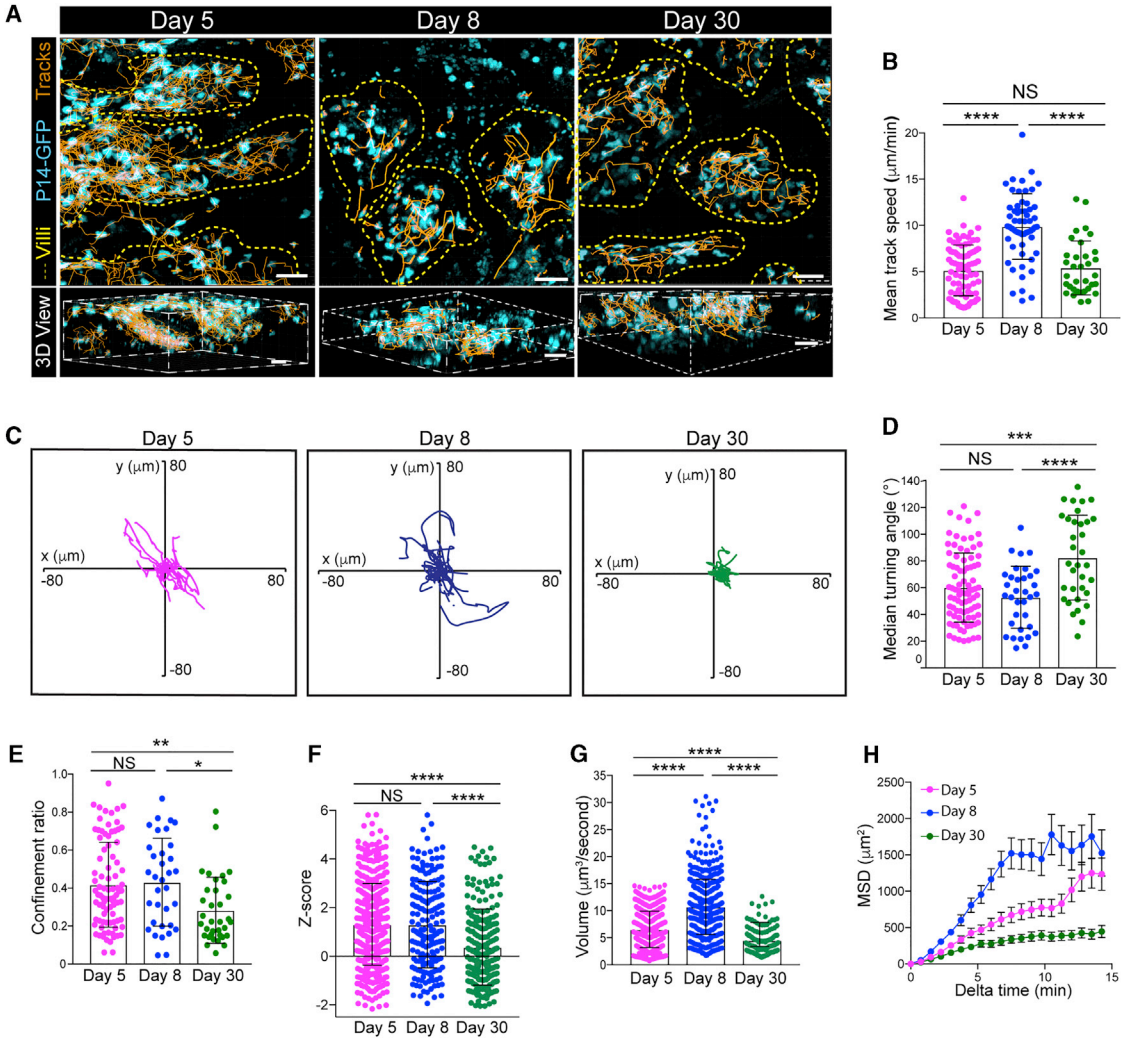

Figure 1. Ag-Specific CD8 T Cell Motility in the Small Intestine Varies during LCMV Infection

Naive P14-GFP CD8 T cells were transferred to B6 mice and infected with LCMV.

(A) Cell tracks (orange) of P14-GFP CD8 T cells (cyan) in the villi (outlined in yellow dashed lines) of the jejunum at the indicated time points after LCMV infection in orthogonal (top) or perspective (bottom) presentation. Scale bar, 20 μm (top) and 30 μm (bottom).

(B–H) Mean track speed (B), flower plots of cell track displacements (C), median turning angle (D), confinement ratio (E), Z straightness (F), volume scanned (G), and mean squared displacement (MSD) (H) as a function of time of P14-GFP CD8 T cells in the villi at days 5 (magenta), 8 (blue), and 30 (green) after LCMV infection.

Dots in motility graphs represent the individual cells imaged. Data of motility parameters presented in bar graphs are derived from the same mouse at the time point indicated. Data are representative of two or more experiments, with mice totaling n = 4 for day 5, n = 7 for day 8, and n = 8 for day 30. A one-way ANOVA with Dunn's multiple comparison test was performed to evaluate statistical significance. *p = 0.01, **p = 0.006, ***p ≤ 0.0003, and ****p ≤ 0.0001. Error bars, SDs. See also Figure S1.

imaging was common and made quantification of cell movement between the epithelium and LP difficult, as well as delineating motility of T cells confined to those areas. Day 5 effector P14-GFP CD8 T cells moved at ~5 μm/min and, by day 8, their speed increased nearly 1.5-fold (Figures 1B and S1D; Video S1). Effector T cells are large to keep up with cellular demands early after infection (4–8 days). We saw that T cells were most highly motile at day 8 following infection, even though they were quite large, indicating that cell size did not hinder T cell locomotion. At memory, when most CD8 T cells become T_{RM}, their speed was significantly slower than at day 8 (Figures 1B and S1D; Videos S1 and S2). The migration of effector CD8 T cells was also assessed in an intact anesthetized mouse using an OT-I-GFP/vesicular stomatitis virus encoding ovalbumin (VSV-OVA) infection model, and similar behaviors were observed (Video S3).

Normalizing T cell tracks to the same point of origin showed that early (day 5) and peak (day 8) effector CD8 T cell tracks were not constrained in any direction; however, T_{RM} were restrained (Figure 1C). This was further verified by a greater median turning angle and lower confinement ratio of T_{RM}

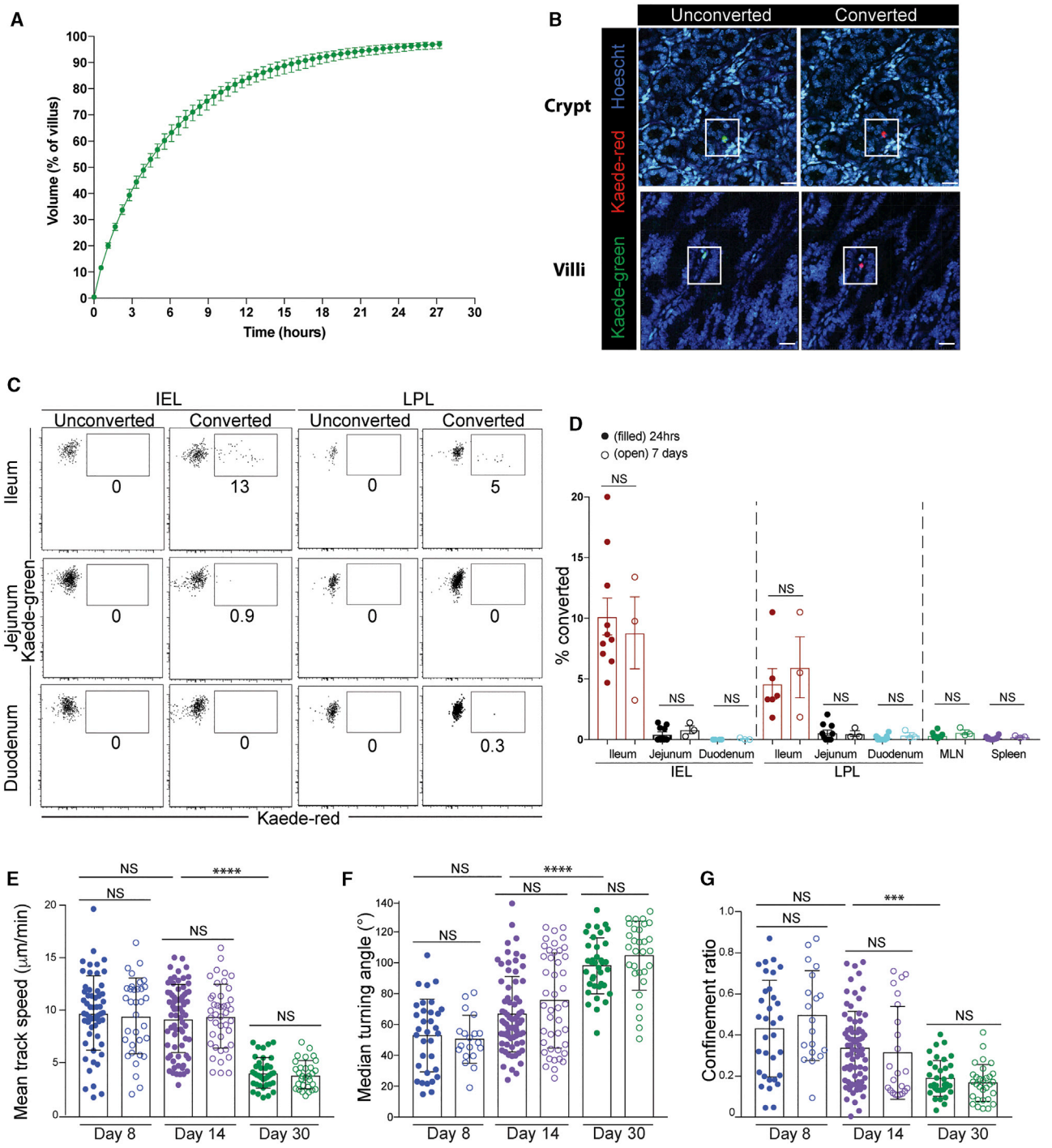

Figure 2. CD8 T_{RM} Have Restricted Locomotion in the Small Intestine

(A) Modeling of 60 P14 CD8 T_{RM} scanning a single villus. Data shown are the time taken to scan the indicated portion of the villus by 60 P14. Error bars show the maximum and minimum volume patrolled over 100 simulations at a specific time.

(B–D) A section of the ileum of OT-I/Kaede memory mice was exposed to 405 nm light. One or 7 days later, portions of the SI were evaluated for converted OT-I/Kaede cells.

(B) Unconverted (green) or converted (red) OT-I/Kaede T cells were visualized in the SI ± light exposure. Scale bar, 20 μm.

(C) Flow cytometric analysis of OT-I/Kaede IEL and LPL in the indicated sections of the intestine 24 h after conversion. Plots are gated on OT-I CD8 T cells. Sham surgery mice were used as unconverted controls.

(legend continued on next page)

compared to effector T cells (Figures 1D, 1E, S1E, and S1F). The turning angle measures the angle at which a cell deviates from its direction of travel. A high turning angle indicates that a cell is turning sharply, while a lower turning angle indicates that the cell is continuing in a similar direction of travel (less restricted). The confinement ratio measures the displacement of the cell divided by its path length. Displacement is a measurement of the shortest distance between an initial point and the final position. Therefore, cells with more restricted motility have a lower confinement ratio, as this indicates minimal displacement over a longer path length (Cahalan and Parker, 2008; Germain et al., 2012). We also assessed the "straightness" of cell tracks using a previously described *Z* score metric, which determines whether experimental displacement is less than ("confined tracks") or higher than ("straight tracks") what is expected by chance (Mrass et al., 2017). T_{RM} tracks had the lowest *Z* score of any time point measured, suggesting that memory T cell motility is more constrained than effector P14 CD8 T cells (Figure 1F). Accordingly, memory T cells also scanned a significantly lower volume than did effector CD8 T cells in the SI and did not exhibit directed migration, as determined by mean squared displacement (MSD) (Figures 1G and 1H). These results suggest that, in contrast to effector CD8 T cells, memory CD8 T cells display markedly confined motility.

T_{RM} Migration in the SI Is Locally Restricted and Independent of CD103

Our imaging analysis showed that memory CD8 T cells scanned a smaller volume of tissue compared to effector CD8 T cells, which suggested that this may affect the efficiency of immune surveillance in this tissue (Figure 1). To understand the surveillance requirement in a villus, we performed mathematical modeling based on our various assessed parameters for T_{RM} movement. Our model estimated that it would take nearly 28 h for 60 CD8 T_{RM} to completely scan a single villus and approximately 1 month for a single T_{RM} to do the same (Figures 2A and S2A). However, our experiments could not distinguish whether CD8 T cell populations are fixed in a particular location of the SI over time or whether there is migration of T cells between areas. To test this, we used the Kaede reporter mouse, which allows the tracking of cells after *in vivo* labeling through photoconversion (Tomura et al., 2008). The establishment of OT-I/Kaede T_{RM} was confirmed via parabiosis (Figure S2B). A piece of the ileum of OT-I/Kaede memory mice was surgically exteriorized and exposed to a 405-nm light for photoconversion, and the position of converted T cells was assessed after 1 or 7 days (Figures 2B and S2C). Photoconverted OT-I/Kaede IEL and LPL (Kaede-red) were present in the ileum of mice exposed to violet light, but remained undetectable in sham surgery controls. Very few (<1%) converted OT-I/Kaede CD8 T cells were detected in the jejunum, duodenum, spleen, or mesenteric lymph node (MLN), and no significant differences in the frequency of converted cells were observed between 24 h and 7 days (Figures 2C, 2D, and S2D). These data indicate that memory CD8 T cells in the SI are limited to surveying relatively narrow areas. In a separate experiment, TPLSM was performed on the ileum of OT-I/Kaede mice before and after conversion, verifying that light exposure did not affect T cell motility (data not shown).

We next wondered what was responsible for the confined motility of T_{RM}s in the SI. In both the skin and liver, CD8 T cell interactions with integrins have been shown to be important for T cell behavior (McNamara et al., 2017; Overstreet et al., 2013; Santamaria Babi et al., 1995). We speculated that CD103 interaction with E-cadherin may be responsible, as this is crucial for T_{RM} maintenance in the epithelium of the SI and heightened expression of CD103 (along with CD69) upon memory formation correlated with restricted motility (Figures S3A and S3B) (Casey et al., 2012). No changes in motility were observed between CD103 sufficient and deficient P14 CD8 T cells at any time point (days 8, 14, and 30) evaluated (Figures 2E–2G and S3C–S3F; Video S4). It was difficult to assess whether the absence of CD103 affected intraepithelial migration and probing, as Hoechst dye could not be used due to spectral overlap, and second harmonic generation (SHG) does not clearly distinguish between the LP and the epithelium. Similar results were observed with experiments using RGD peptides to block interactions between integrins and several components of the extracellular matrix (ECM) (data not shown). These results suggest that integrins do not contribute to T_{RM} locomotion.

SI Tissue Architecture Dictates CD8 T Cell Motility

Tissue composition can affect CD8 T cell motility (Germain et al., 2012; Overstreet et al., 2013; Sorokin, 2010). We inquired whether the complex and unique tissue architecture of the SI could affect CD8 T cell interstitial migration. The SI can be divided into four unique layers: serosa, *muscularis externa*, submucosa, and mucosa (Figure 3A) (Mowat and Agace, 2014; Wright et al., 1989). In the serosa and longitudinal muscle, P14-GFP CD8 T cells were elongated parallel to myocytes, while T cells in the less dense circular muscle maintained an amoeboid shape (Figures 3B and 3C; Videos S5 and S6). At both days 5 and 8, P14-GFP CD8 T cells in the *muscularis externa* had shorter path lengths and were slower and more confined, as compared to CD8 T cells in the crypts (Figures 3D–3H; Videos S5, S6, and S7). The volume scanned by P14-GFP CD8 T cells increased

(D) Frequency of photoconverted cells (Kaede, red) in indicated locations 24 h (filled) and day 7 (open) after conversion. A Mann-Whitney test was used to evaluate significance. Data are representative of three experiments, n = 10 mice. Error bars, SEMs.
(E–G) Naive P14-GFP and P14/CD103$^{-/-}$-CFP CD8 T cells were transferred to B6 mice and infected with LCMV. (E) Mean track speed, (F) median turning angle, and (G) confinement ratio of P14-GFP and P14-CFP CD8 T cells at day 8 (blue), day 14 (purple), and day 30 (green). Filled circles, WT P14-GFP; open circles, P14/CD103$^{-/-}$-CFP.
Dots in motility graphs represent individual cells imaged. Data of motility parameters presented in bar graphs are derived from the same mouse at the time point indicated. Data are representative of two experiments, with mice totaling n = 5 for day 8, n = 5 for day 14, and n = 4 for day 30. A Kruskal-Wallis one-way ANOVA with Dunn's multiple comparison test was performed to evaluate statistical significance. ***p = 0.007 and ****p $\leq$ 0.0001. Error bars, SDs.
See also Figures S2 and S3.

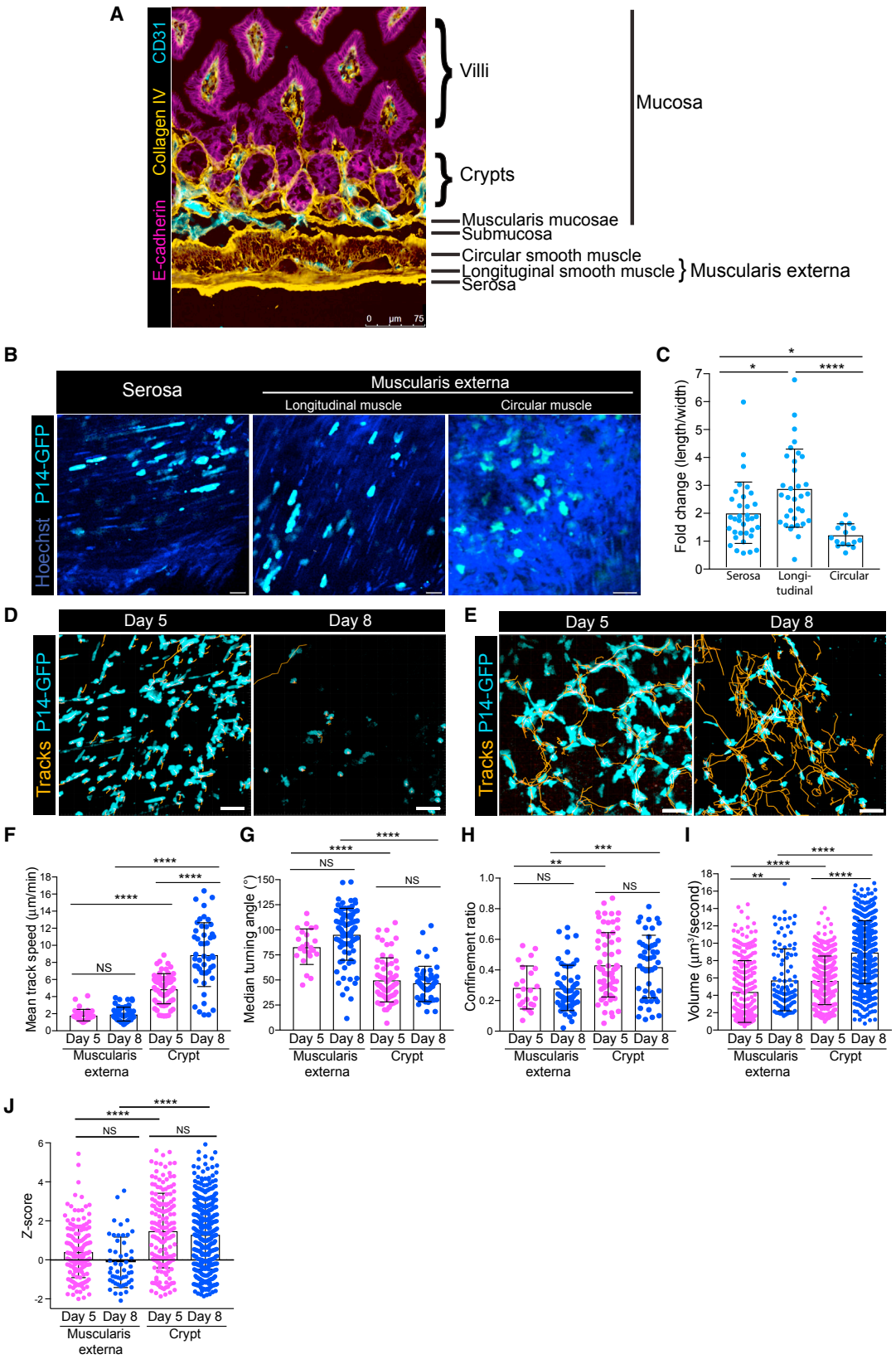

(legend on next page)

between days 5 and 8 in both the serosa and the crypt, without a change in confinement measurements (Figure 3I). CD8 T cells in the crypt often orbited around its entire planar section. Alternatively, effector CD8 T cells in the serosa exhibited low *Z* scores, indicating confined motile behavior (Figure 3J). T_{RM}s were nearly completely absent from the serosa and crypt, which suggests that P14 T cells are excluded from those compartments after LCMV infection subsides. These results indicate that Ag-specific CD8 T cells in the SI rely on the immediate tissue architecture to influence their migratory pattern.

Inflammation Alters T_{RM} Patrolling Behavior

Reports indicate that inflammation can cause alterations to tissue architecture that can affect T cell migration (Hallmann et al., 2015; Mueller et al., 2007a, 2007b; Zaid et al., 2014). Since we observed striking differences in motility based on the location of CD8 T cells within the SI, we wondered whether bystander inflammation could drive changes in T_{RM} motility, possibly due to the reorganization of the ECM. P14-GFP CD8 T cell memory mice received naive OT-I-CFP CD8 T cells and were orally infected with *Yersinia pseudotuberculosis* expressing OVA (Yptb-OVA) (Figure 4A) (Bergsbaken and Bevan, 2015). At day 6 following Yptb-OVA infection, the speed of P14-GFP CD8 T_{RM} was not altered by bystander inflammation; however, these T cells were less constrained as compared to the steady state. Their turning angle was significantly decreased and the confinement ratio was slightly increased (Figures 4B–4D and S4A–S4C; Video S8). Effector OT-I-CFP T cells exhibited a migration pattern that is comparable to effector P14-GFP CD8 T cells following LCMV (Figures 4B–4D; Video S8). While bystander inflammation has some impact on memory T cell motility, T_{RM} do not match the motility of effector T cells in the very same inflammatory environment, suggesting that some behaviors are Ag driven or cell intrinsic. We next tested the impact of acute inflammation on P14-GFP CD8 T_{RM} behavior using lipopolysaccharide (LPS)-induced endotoxemia. T_{RM} became more restricted in comparison to steady-state conditions, having a wider turning angle (Figures 4E–4G and S4D–S4F; Video S9). These results show that the motility of T_{RM} in response to various types of inflammation is dynamic.

As the SI is a portal of microbial entry, it needs to maintain active immune surveillance; however, it must also curtail inappropriate immune responses to self-protein, normal flora, and food Ag (Konjar et al., 2017). We next addressed whether the motility of self-specific CD8 T cells would be affected by the presence of auto-Ag in the SI. We used mice that produce OVA under the control of the intestinal fatty acid-binding protein promoter (iFABP-OVA), which limits OVA expression to mature enterocytes of the SI (Vezys et al., 2000). Five days after transfer, tolerant OT-I cells were detected in the LP and the epithelium in large numbers and displayed slowed migration speed (~4 μm/min) with frequent arrests (Figures 4H and S4G–S4L) (Pauken et al., 2015). Arrest was due to the presence of Ag, as blocking K^b-SIINFEKL complexes resulted in significantly increased mean track speed (Figure 4H; Video S10). However, this did not affect other measurements of motility (Figures 4I, 4J, and S4L; Video S10). At day 10 following transfer, when tolerance is more established, OT-I-GFP CD8 T cells migrated at a 2-fold higher speed in comparison to day 5 OT-I-GFP CD8 T cells and were not affected when interactions with the Ag were blocked (Figures S4G–S4O). These data indicate that, as T cells fully differentiate to a tolerant state, they become incapable of Ag interaction, which affects their motility.

DISCUSSION

The expansive and ever-changing milieu of the gut likely necessitates plastic and adaptable T cell motility to achieve effective immune surveillance of this compartment. The constant balance between activation and suppression makes the SI perhaps the most dynamic immune environment in the host (Chistiakov et al., 2015; Cieza et al., 2012). We found that Ag-specific CD8 T cell motility in the SI varied greatly, depending on the presence of Ag, the inflammatory context, and the surrounding tissue architecture. The initial arrest of T cells at early time points after infection was likely due to T cell receptor (TCR) engagement with Ag, signaling the cell to slow down (Figures 1 and S1) (Celli et al., 2011; Dustin et al., 1997). The increase in speed at day 8 may be to optimize T cell scanning once local Ag is cleared, as the volume scanned by P14 CD8 T cells was greatest at this time point in the crypts and villi (Müller et al., 2000). Similar observations have been made in many solid tumor models (Boissonnas et al., 2007; Breart et al., 2008; Mrass et al., 2006).

In contrast, CD8 T_{RM} were highly confined, even given the need to survey such an expansive environment (Figures 1 and S1). This was not observed in T_{RM} found in the female reproductive tract or liver, where T cells are highly motile (Beura et al., 2018; Fernandez-Ruiz et al., 2016). While we suspected that the CD103 integrin may be responsible for this restricted T cell

Figure 3. Tissue Architecture Dictates CD8 T Cell Motility in the Small Intestine

(A) Histological section of SI jejunum stained with E-cadherin (magenta), collagen IV (yellow), and CD31 (cyan). Scale bar, 75 μm.

(B) P14-GFP CD8 T cells were transferred to B6 and infected with LCMV. Five days post-infection, P14-GFP CD8 T cells (cyan) in the serosa and *muscularis externa* were imaged using TPLSM. Hoechst stain (dark blue) was injected before imaging.

(C) Fold change of length over width measurements of individual P14-GFP CD8 T cells in the serosa, longitudinal muscle, and circular muscle at day 5 after LCMV.

(D) Cell tracks (orange) of P14-GFP CD8 T cells (cyan) in the *muscularis externa* and serosa at days 5 and 8 after LCMV infection.

(E) Same as in (D), but in crypts of SI.

(F–J) Mean track speed (F), median turning angle (G), confinement ratio (H), volume scanned (I), and *Z* score (J) of P14-GFP CD8 T cells at days 5 (magenta) and 8 (blue) after LCMV infection in the indicated locations of the SI.

Scale bars in (B), (D), and (E), 20 μm. Dots in motility graphs represent individual cells imaged. Data of motility parameters for each specific experiment presented in bar graphs are derived from the same mouse at the time point indicated. Data are representative of at least two experiments, with mice totaling n = 4 for day 5 and n = 5 for day 8 in the *muscularis externa*, and n = 5 for day 5 and n = 7 for day 8 in the crypt. A Kruskal-Wallis one-way ANOVA with Dunn's multiple comparison test was performed to evaluate statistical significance. *$p \leq 0.05$, **$p \leq 0.003$, ***$p = 0.0003$, and ****$p \leq 0.0001$. All error bars, SDs.

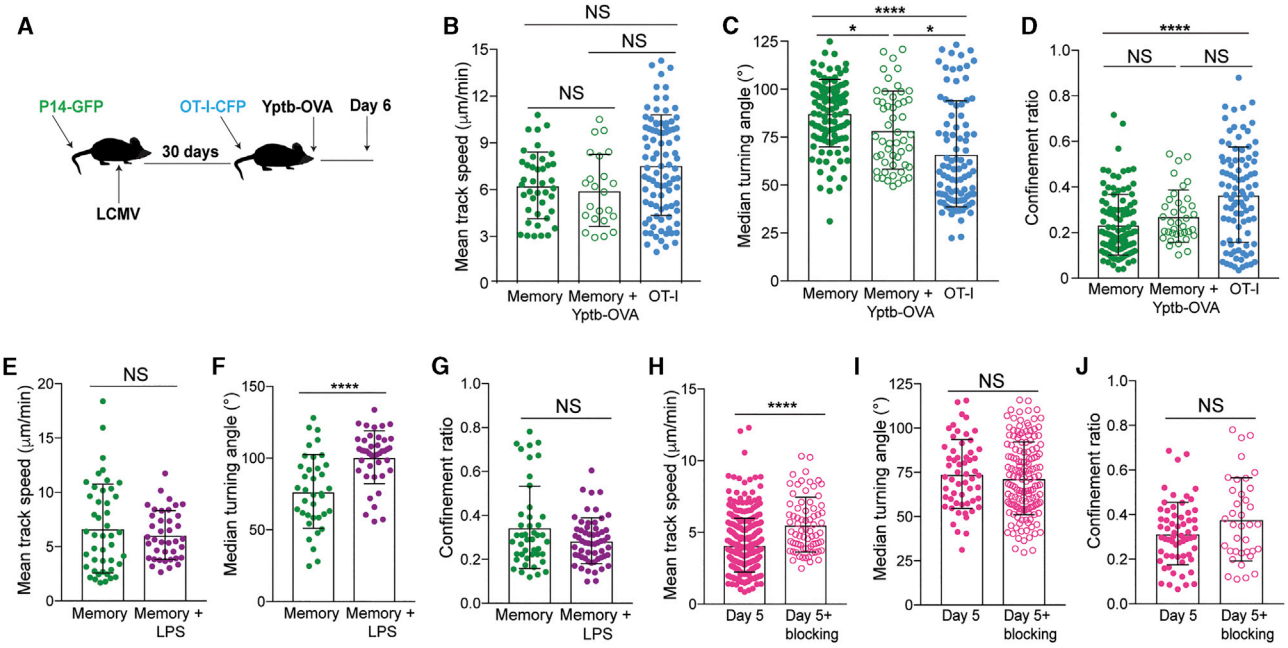

Figure 4. Bystander Inflammation Affects CD8 T_{RM} Motility

(A–D) Memory P14-GFP mice received OT-I-CFP CD8 T cells and were orally infected with Yptb-OVA 1 day later. Cells were imaged in the jejunum 6 days later. (A) Experimental setup, (B) mean track speed, (C) median turning angle, and (D) confinement ratio of memory P14-GFP CD8 T during Yptb-OVA infection (green, open) and day 6 OT-I-CFP CD8 T cells (blue, filled), compared to steady-state P14-GFP memory CD8 T cells (green, filled). Data are representative of at least two experiments totaling n = 4 mice for experiments with Yptb-OVA and n = 4 mice for experiments with memory at steady state. A Kruskal-Wallis one-way ANOVA with Dunn's multiple comparison test was performed to evaluate statistical significance. *$p \leq 0.05$ and ****$p \leq 0.0001$.

(E–G) Memory P14-GFP mice were injected intraperitoneally with 4 mg/kg LPS and imaged 4–5 h later. (E) Mean track speed, (F) turning angle, and (G) confinement ratio of P14-GFP CD8 T cells in the absence (green) or presence (purple) of LPS. Experiments are representative of n = 4 memory + LPS mice and n = 2 memory mice. Mann-Whitney tests were used to evaluate significance. ****$p \leq 0.0001$.

(H–J) OT-I-GFP CD8 T cells were transferred to iFABP-OVA mice and evaluated 5 days after transfer ± K^b-SIINFEKL blocking antibody. (H) Mean track speed, (I) median turning angle, and (J) confinement ratio of day 5 (magenta, filled) and day 5 + blocking Ab (magenta, open) OT-I-GFP CD8 T cells.

Data represent at least two experiments, n = 3 mice without blocking and n = 3 mice with blocking. Mann-Whitney tests were performed to evaluate statistical significance. ****$p \leq 0.0001$. All error bars, SDs. In all graphs measuring motility, dots represent individual cells imaged. Data of motility parameters for each specific experiment presented in bar graphs are derived from the same mouse at the time point indicated.

See also Figure S4.

behavior at memory time points in the SI, the loss of CD103 in P14 CD8 T cells had no impact on T cell locomotion (Figures 2E–2G and S3C–S3F). It is likely that the architecture of the SI supersedes targeted motility; for example, the most direct route from one point to another may be by "space walking" across the intestinal lumen, which we did not observe. To this point, CD8 T cells were confined to orbiting crypts and circling within villi. In addition, results from MSD indicated that the cells in the villi were not directed and exhibited more of a Brownian motion (Figure 1H). As CD8 T cell motility in the SI was not mediated by integrins, we wondered whether confinement was due to the reorganization of the ECM after infection subsides. This could be similar to effector CD8 T cells in the muscularis layer of the SI, which were seemingly held between muscle cells and potentially confined because of this (Figure 3). Throughout the course of infection, the ECM can be considerably reorganized, and differences in tissue architecture can affect T cell motility (Overstreet et al., 2013; Sorokin, 2010). At day 14 after LCMV infection, T cells exhibited motility that was midway between days 8 and 30 (Figures S1D–S1F). During an antigenically distinct local infection with Yptb-OVA or introduction of LPS, T_{RM} motility was disparately affected (Figures 4 and S4A–S4F). This indicates that CD8 T cells adapt their migratory behavior depending on various inflammatory cues. Effector T cells in the same environment displayed distinct locomotion, as compared to bystander memory T cells, validating that certain behaviors are Ag driven and/or are intrinsic to effector T cells. At day 5, self-specific CD8 T cells were slightly more confined and slower than P14 CD8 T cells at effector time points (Figures 1 and 4H–4J). This enforces the concept that the less hindered mobility of effector T cells could be due to microbial-induced inflammation and tissue restructuring, as OT-I transfer to iFABP-OVA mice does not induce high levels of inflammation (Vezys et al., 2000).

Our studies demonstrate that CD8 T cell mobility in the SI is disparate throughout the course of infection and may be governed by the complex tissue architecture of the SI. Interactions with integrins do not affect CD8 T cell motility, but T_{RM} locomotion is influenced by the local inflammatory milieu. This work informs the requirements for therapies that are dependent on efficient CD8 T cell immune surveillance of the SI and suggests that,

given their restricted motile behavior, large numbers of CD8 T_{RM} in the SI are required for effective immunity against microbes and malignancies.

STAR★METHODS

Detailed methods are provided in the online version of this paper and include the following:

- KEY RESOURCES TABLE
- CONTACT FOR REAGENT AND RESOURCE SHARING
- EXPERIMENTAL MODEL AND SUBJECT DETAILS
- METHOD DETAILS
  - Infections
  - Parabiotic surgery
  - Photoconversion of OT-I/Kaede CD8 T cells
  - Tissue harvesting and processing
  - Tissue freezing, immunofluorescence and microscopy
  - Flow cytometry and peptide stimulation
  - Two-photon laser scanning microscopy and analysis
- QUANTIFICATION AND STATISTICAL ANALYSIS

SUPPLEMENTAL INFORMATION

Supplemental Information includes four figures and ten videos and can be found with this article online at https://doi.org/10.1016/j.celrep.2019.02.034.

ACKNOWLEDGMENTS

We would like to thank Dr. J. Michael Stolley for schematic artistry; Dr. Mark J. Miller for help with SI TPLSM development; Drs. Yoji Shimizu and Brandon Burbach for providing OT-I-GFP mice; and Drs. Stephen Jameson, Kris Hogquist, and Tessa Bergsbaken for sharing Kaede transgenic mice and Yptb-OVA. This work was funded by a University of Minnesota Academic Health Center Seed Grant (to V.V.), NIH grant T32AI007313 (to E.A.T.), and by the University of Minnesota Doctoral Dissertation Fellowship (to E.A.T.). B.T.F. and J.S.M. are supported by NIH R01 AI106791 and P01 AI35296. D.J.T. is supported by NIH UTEP BUILDing SCHOLARS award RL5GM118969 and an NIH Institutional Development Award (IDeA) P20GM1034. D.M. is supported by NIH R01 AI084913.

AUTHOR CONTRIBUTIONS

E.A.T., J.S.M., L.K.B., and M.J.P. performed the experiments and analyzed the data. P.M., D.J.T., and J.L.C. calculated the parameters of motility and performed the modeling experiments. E.A.T., L.K.B., B.T.F., D.M., and V.V. designed the experiments. E.A.T. and V.V. wrote the manuscript.

DECLARATION OF INTERESTS

The authors declare no competing interests.

Received: February 19, 2018
Revised: August 5, 2018
Accepted: February 8, 2019
Published: March 12, 2019

REFERENCES

Bergsbaken, T., and Bevan, M.J. (2015). Proinflammatory microenvironments within the intestine regulate the differentiation of tissue-resident CD8$^+$ T cells responding to infection. Nat. Immunol. *16*, 406–414.

Bergsbaken, T., Bevan, M.J., and Fink, P.J. (2017). Local Inflammatory Cues Regulate Differentiation and Persistence of CD8$^+$ Tissue-Resident Memory T Cells. Cell Rep. *19*, 114–124.

Beura, L.K., Anderson, K.G., Schenkel, J.M., Locquiao, J.J., Fraser, K.A., Vezys, V., Pepper, M., and Masopust, D. (2015). Lymphocytic choriomeningitis virus persistence promotes effector-like memory differentiation and enhances mucosal T cell distribution. J. Leukoc. Biol. *97*, 217–225.

Beura, L.K., Mitchell, J.S., Thompson, E.A., Schenkel, J.M., Mohammed, J., Wijeyesinghe, S., Fonseca, R., Burbach, B.J., Hickman, H.D., Vezys, V., et al. (2018). Intravital mucosal imaging of CD8$^+$ resident memory T cells shows tissue-autonomous recall responses that amplify secondary memory. Nat. Immunol. *19*, 173–182.

Boissonnas, A., Fetler, L., Zeelenberg, I.S., Hugues, S., and Amigorena, S. (2007). In vivo imaging of cytotoxic T cell infiltration and elimination of a solid tumor. J. Exp. Med. *204*, 345–356.

Breart, B., Lemaître, F., Celli, S., and Bousso, P. (2008). Two-photon imaging of intratumoral CD8$^+$ T cell cytotoxic activity during adoptive T cell therapy in mice. J. Clin. Invest. *118*, 1390–1397.

Cahalan, M.D., and Parker, I. (2008). Choreography of cell motility and interaction dynamics imaged by two-photon microscopy in lymphoid organs. Annu. Rev. Immunol. *26*, 585–626.

Casey, K.A., Fraser, K.A., Schenkel, J.M., Moran, A., Abt, M.C., Beura, L.K., Lucas, P.J., et al. (2012). Antigen-independent differentiation and maintenance of effector-like resident memory T cells in tissues. J. Immunol. *188*, 4866–4875.

Celli, S., Albert, M.L., and Bousso, P. (2011). Visualizing the innate and adaptive immune responses underlying allograft rejection by two-photon microscopy. Nat. Med. *17*, 744–749.

Chistiakov, D.A., Bobryshev, Y.V., Kozarov, E., Sobenin, I.A., and Orekhov, A.N. (2015). Intestinal mucosal tolerance and impact of gut microbiota to mucosal tolerance. Front. Microbiol. *5*, 781.

Cieza, R.J., Cao, A.T., Cong, Y., and Torres, A.G. (2012). Immunomodulation for gastrointestinal infections. Expert Rev. Anti Infect. Ther. *10*, 391–400.

Dustin, M.L., Bromley, S.K., Kan, Z., Peterson, D.A., and Unanue, E.R. (1997). Antigen receptor engagement delivers a stop signal to migrating T lymphocytes. Proc. Natl. Acad. Sci. USA *94*, 3909–3913.

Edelblum, K.L., Shen, L., Weber, C.R., Marchiando, A.M., Clay, B.S., Wang, Y., Prinz, I., Malissen, B., Sperling, A.I., and Turner, J.R. (2012). Dynamic migration of γδ intraepithelial lymphocytes requires occludin. Proc. Natl. Acad. Sci. USA *109*, 7097–7102.

Fernandez-Ruiz, D., Ng, W.Y., Holz, L.E., Ma, J.Z., Zaid, A., Wong, Y.C., Lau, L.S., Mollard, V., Cozijnsen, A., Collins, N., et al. (2016). Liver-Resident Memory CD8$^+$ T Cells Form a Front-Line Defense against Malaria Liver-Stage Infection. Immunity *45*, 889–902.

Fife, B.T., Pauken, K.E., Eagar, T.N., Obu, T., Wu, J., Tang, Q., Azuma, M., Krummel, M.F., and Bluestone, J.A. (2009). Interactions between PD-1 and PD-L1 promote tolerance by blocking the TCR-induced stop signal. Nat. Immunol. *10*, 1185–1192.

Germain, R.N., Robey, E.A., and Cahalan, M.D. (2012). A decade of imaging cellular motility and interaction dynamics in the immune system. Science *336*, 1676–1681.

Hallmann, R., Zhang, X., Di Russo, J., Li, L., Song, J., Hannocks, M.-J., and Sorokin, L. (2015). The regulation of immune cell trafficking by the extracellular matrix. Curr. Opin. Cell Biol. *36*, 54–61.

Hoytema van Konijnenburg, D.P., Reis, B.S., Pedicord, V.A., Farache, J., Victora, G.D., and Mucida, D. (2017). Intestinal Epithelial and Intraepithelial T Cell Crosstalk Mediates a Dynamic Response to Infection. Cell *171*, 783–794.e13.

Konjar, Š., Ferreira, C., Blankenhaus, B., and Veldhoen, M. (2017). Intestinal Barrier Interactions with Specialized CD8 T Cells. Front. Immunol. *8*, 1281.

McDole, J.R., Wheeler, L.W., McDonald, K.G., Wang, B., Konjufca, V., Knoop, K.A., Newberry, R.D., and Miller, M.J. (2012). Goblet cells deliver luminal antigen to CD103+ dendritic cells in the small intestine. Nature *483*, 345–349.

McNamara, H.A., Cai, Y., Wagle, M.V., Sontani, Y., Roots, C.M., Miosge, L.A., O'Connor, J.H., Sutton, H.J., Ganusov, V.V., Heath, W.R., et al. (2017). Up-regulation of LFA-1 allows liver-resident memory T cells to patrol and remain in the hepatic sinusoids. Sci. Immunol. *2*, eaaj1996.

Mowat, A.M., and Agace, W.W. (2014). Regional specialization within the intestinal immune system. Nat. Rev. Immunol. *14*, 667–685.

Mrass, P., Takano, H., Ng, L.G., Daxini, S., Lasaro, M.O., Iparraguirre, A., Cavanagh, L.L., von Andrian, U.H., Ertl, H.C., Haydon, P.G., and Weninger, W. (2006). Random migration precedes stable target cell interactions of tumor-infiltrating T cells. J. Exp. Med. *203*, 2749–2761.

Mrass, P., Oruganti, S.R., Fricke, G.M., Tafoya, J., Byrum, J.R., Yang, L., Hamilton, S.L., Miller, M.J., Moses, M.E., and Cannon, J.L. (2017). ROCK regulates the intermittent mode of interstitial T cell migration in inflamed lungs. Nat. Commun. *8*, 1010.

Mueller, S.N., Hosiawa-Meagher, K.A., Konieczny, B.T., Sullivan, B.M., Bachmann, M.F., Locksley, R.M., Ahmed, R., and Matloubian, M. (2007a). Regulation of homeostatic chemokine expression and cell trafficking during immune responses. Science *317*, 670–674.

Mueller, S.N., Matloubian, M., Clemens, D.M., Sharpe, A.H., Freeman, G.J., Gangappa, S., Larsen, C.P., and Ahmed, R. (2007b). Viral targeting of fibroblastic reticular cells contributes to immunosuppression and persistence during chronic infection. Proc. Natl. Acad. Sci. USA *104*, 15430–15435.

Müller, S., Bühler-Jungo, M., and Mueller, C. (2000). Intestinal intraepithelial lymphocytes exert potent protective cytotoxic activity during an acute virus infection. J. Immunol. *164*, 1986–1994.

Overstreet, M.G., Gaylo, A., Angermann, B., Hughson, A., Hyun, Y., Lambert, K., Acharya, M., Billroth-Maclurg, A.C., Rosenberg, A.F., Topham, D.J., et al. (2013). Inflammation-induced effector $CD4^+$ T cell interstitial migration is alpha-v integrin dependent. Nat. Immunol. *14*, 949–958.

Pauken, K.E., Nelson, C.E., Martinov, T., Spanier, J.A., Heffernan, J.R., Sahli, N.L., Quarnstrom, C.F., et al. (2015). Cutting edge: identification of autoreactive CD4+ and CD8+ T cell subsets resistant to PD-1 pathway blockade. J. Immunol. *194*, 3551–3555.

Santamaria Babi, L.F., Moser, R., Perez Soler, M.T., Picker, L.J., Blaser, K., and Hauser, C. (1995). Migration of skin-homing T cells across cytokine-activated human endothelial cell layers involves interaction of the cutaneous lymphocyte-associated antigen (CLA), the very late antigen-4 (VLA-4), and the lymphocyte function-associated antigen-1 (LFA-1). J. Immunol. *154*, 1543–1550.

Schenkel, J.M., Fraser, K.A., Vezys, V., and Masopust, D. (2013). Sensing and alarm function of resident memory $CD8^+$ T cells. Nat. Immunol. *14*, 509–513.

Sorokin, L. (2010). The impact of the extracellular matrix on inflammation. Nat. Rev. Immunol. *10*, 712–723.

Steinert, E.M., Schenkel, J.M., Fraser, K.A., Beura, L.K., Manlove, L.S., Igyártó, B.Z., Southern, P.J., and Masopust, D. (2015). Quantifying Memory CD8 T Cells Reveals Regionalization of Immunosurveillance. Cell *161*, 737–749.

Sujino, T., London, M., Hoytema van Konijnenburg, D.P., Rendon, T., Buch, T., Silva, H.M., Lafaille, J.J., Reis, B.S., and Mucida, D. (2016). Tissue adaptation of regulatory and intraepithelial $CD4^+$ T cells controls gut inflammation. Science *352*, 1581–1586.

Sumida, H., Lu, E., Chen, H., Yang, Q., Mackie, K., and Cyster, J.G. (2017). GPR55 regulates intraepithelial lymphocyte migration dynamics and susceptibility to intestinal damage. Sci. Immunol. *2*, eaao1135.

Thompson, E.A., Beura, L.K., Nelson, C.E., Anderson, K.G., and Vezys, V. (2016). Shortened Intervals during Heterologous Boosting Preserve Memory CD8 T Cell Function but Compromise Longevity. J. Immunol. *196*, 3054–3063.

Tomura, M., Yoshida, N., Tanaka, J., Karasawa, S., Miwa, Y., Miyawaki, A., and Kanagawa, O. (2008). Monitoring cellular movement in vivo with photoconvertible fluorescence protein "Kaede" transgenic mice. Proc. Natl. Acad. Sci. USA *105*, 10871–10876.

Vezys, V., Olson, S., and Lefrançois, L. (2000). Expression of intestine-specific antigen reveals novel pathways of CD8 T cell tolerance induction. Immunity *12*, 505–514.

Wang, X., Sumida, H., and Cyster, J.G. (2014). GPR18 is required for a normal $CD8\alpha\alpha$ intestinal intraepithelial lymphocyte compartment. J. Exp. Med. *211*, 2351–2359.

Wright, N.A., Carter, J., and Irwin, M. (1989). The measurement of villus cell population size in the mouse small intestine in normal and abnormal states: a comparison of absolute measurements with morphometric estimators in sectioned immersion-fixed material. Cell Tissue Kinet. *22*, 425–450.

Xu, C., Shen, Y., Littman, D.R., Dustin, M.L., and Velázquez, P. (2012). Visualization of mucosal homeostasis via single- and multiphoton intravital fluorescence microscopy. J. Leukoc. Biol. *92*, 413–419.

Zaid, A., Mackay, L.K., Rahimpour, A., Braun, A., Veldhoen, M., Carbone, F.R., Manton, J.H., Heath, W.R., and Mueller, S.N. (2014). Persistence of skin-resident memory T cells within an epidermal niche. Proc. Natl. Acad. Sci. USA *111*, 5307–5312.

STAR★METHODS

KEY RESOURCES TABLE

REAGENT or RESOURCE	SOURCE	IDENTIFIER
Antibodies		
PE/Cy7 anti-CD8α antibody (53-6.7)	BioLegend	Catalog# 100722; RRID:AB_312761
Brilliant violet 605 anti-CD8α antibody (53-6.7)	BioLegend	Catalog# 100744; RRID:AB_2562609
Alexa fluor 700 anti-CD44 antibody (IM7)	BioLegend	Catalog# 103026; RRID: AB_493713
Brilliant violet 785 anti-CD44 antibody (IM7)	BioLegend	Catalog# 103059; RRID: AB_2571953
PerCP/Cy5.5 anti-CD45.1 antibody (A20)	TONBO Biosciences	Catalog# 65-0453-U100; RRID: AB_2621893
PE anti-CD69 antibody (H1.2F3)	ebioscience-ThermoFisher	Catalog#12-0691-82; RRID:AB_465732
PE/Cy7 anti-CD69 antibody (H1.2F3)	ebioscience-ThermoFisher	Catalog# 25-0691-82; RRID:AB_469637
PE-CF594 anti-CD69 antibody (H1.2F3)	BD Biosciences	Catalog# 562455; RRID:AB_11154217
efluor 450 anti-CD90.1 antibody (HIS51)	ebioscience-ThermoFisher	Catalog# 48-0900-82; RRID:AB_1272254
Brilliant violet 510 anti-CD103 antibody (M290)	BD Biosciences	Catalog# 563087; RRID:AB_2721775
FITC anti-CD103 antibody (2E7)	BioLegend	Catalog# 121420; RRID:AB_10714791
InVivoMab anti-K^b-SIINFEKL antibody (25-D1.15)	BioXcell	Catalog# BE0207; RRID:AB_10950697
InVivoMab IgG1 isotype control (MOPC-21)	BioXcell	Catalog# BE0083; RRID:AB_1107784
Alexa fluor 647 anti-Ecadherin antibody (DECMA-1)	BioLegend	Catalog# 147308; RRID:AB_2563955
PE anti-CD31antibody (MEC13.3)	BD Biosciences	Catalog# 561073; RRID:AB_10563931
Unconjugated goat anti-Collagen IV antibody (polyclonal)	Millipore	Catalog# AB769; RRID:AB_11210995
Alexa fluor 488 bovine anti-goat antibody (polyclonal)	Jackson Immunoresearch	Catalog# 805-545-180; RRID:AB_2340883
PerCP/Cy5.5 anti-PD-1 antibody (RMP1- 30)	BioLegend	Catalog# 109120; RRID:AB_2566641
APC anti-IFNγ antibody (XMG1.2)	ebioscience-ThermoFisher	Catalog# 17-7311-82; RRID:AB_469504
Bacterial and Virus Strains		
Lymphocytic choriomeningitis virus (LCMV)- Armstrong strain	Dr. R. Ahmed, Emory University	N/A
Yesinia pseudotuberculosis-OVA	Dr. Stephen Jameson, University of Minnesota and Dr. Tessa L. Bergsbaken, Rutgers University	N/A
Lipopolysaccharides from *Escherichia coli* O111:B4	Sigma-Aldrich	Catalog#L4391
Chemicals, Peptides, and Recombinant Proteins		
H-2Kb -restricted peptide SIINFEKL	New England Peptide (Custom peptide synthesis)	N/A
DL-Dithioerythritol (DTE), Ultra Pure Grade	VWR Scientific	Catalog# 97061-642
4',6-Diamidino-2-Phenylindole dihydrochloride (DAPI)	Sigma Aldrich	Catalog# D9542
Collagenase I	Worthington Biochemicals	Catalog# LS004197
Live dead Ghost Dye Red 780	TONBO Biosciences	Catalog# 13-0865-T500
H-2Db /GP_{33-41} KAVYNFATM biotinylated monomer	Prepared in house following NIAID tetramer core facility protocol	N/A
H-2Kb /$OVA_{257-264}$ SIINFEKL biotinylated monomer	Prepared in house following NIAID tetramer core facility protocol	N/A
Streptavidin-APC (monomer tetramerization)	Life Technologies	Catalog# S868
Streptavidin-PE (monomer tetramerization)	Life Technologies	Catalog# S866
Experimental Models: Organisms/Strains		
C57BL/6J	The Jackson Laboratory	Catalog# JAX:000664; RRID: IMSR_JAX:000664
C57BL/6-Tg (UBC-GFP)30Scha/J (ubiquitin-GFP)	The Jackson Laboratory	Catalog# JAX:004353; RRID:IMSR_JAX:004353

(*Continued on next page*)

Continued

REAGENT or RESOURCE	SOURCE	IDENTIFIER
Tg(CAG-ECFP)CK6Nagy/J (actin-ECFP)	The Jackson Laboratory	Catalog# JAX:004218; RRID:IMSR_JAX:004218
B6.Cg-Tg(Itgax-Venus)1Mnz/J (CD11c-eYFP)	The Jackson Laboratory	Catalog# JAX:008829; RRID:IMSR_JAX:008829
B6.129S29(C)-*Itgae*tm1Cmp/J	The Jackson Laboratory	Catalog# JAX:006144, RRID:IMSR_JAX:006144
iFABP-OVA	Dr. V. Vezys, Univ. of Minnesota	NA
P14	Dr. R. Ahmed, Emory University	Catalog# MUGEN:M189001, RRID: IMSR_MUGEN:M189001
OT-I	Dr. K. Hogquist, Univ. of Minnesota	Catalog# JAX:003831, RRID: IMSR_JAX:003831
Kaede B6	Dr. M. Tomura, RIKEN & Dr. K. Hogquist, Univ. of Minnesota	Catalog# RBRC05737, RRID: IMSR_RBRC05737
B6 CD45.1	Charles River Laboratories	Catalog# CRL:564, RRID: IMSR_CRL:564
B6 Thy1.1	The Jackson Laboratory	Catalog# JAX:000406, RRID: IMSR_JAX:000406
Software and Algorithms		
Flowjo v9 and v10	Treestar Inc	RRID:SCR_008520
Prism 7	Graphpad Inc	RRID:SCR_002798
Imaris v8 and v9	Bitplane	RRID:SCR_007370

CONTACT FOR REAGENT AND RESOURCE SHARING

Further information and requests for resources and reagents should be directed to and will be fulfilled by the Lead Contact, Vaiva Vezys (vvezys@umn.edu).

EXPERIMENTAL MODEL AND SUBJECT DETAILS

C57BL/6J (B6), C57BL/6-Tg (UBC-GFP)30Scha/J (ubiquitin-GFP), Tg(CAG-ECFP)CK6Nagy/J (actin-ECFP), B6.129S2(C)-*Itgae*^{tm1Cmp}/J (CD103KO), B6.Cg-Tg(Itgax-Venus)1Mnz/J, and B6 Thy1.1 mice were purchased from The Jackson Laboratory. B6 CD45.1 mice were purchased from Charles River Laboratories. All mice were maintained in specific pathogen free conditions at the University of Minnesota. iFABP-OVA, P14/CD45.1, and OT-I/CD45.1 mice were bred and maintained in house. Kaede mice were a generous gift from Dr. Kristin Hogquist (University of Minnesota). P14 and OT-I reporter mice were generated by crossing the TCR Tg mice with ubiquitin-GFP or actin-ECFP mice. P14-CFP^{+} CD103$^{-/-}$ mice were generated by crossing P14-CFP^{+} mice to P14^{+} CD103$^{-/-}$ mice. Kaede B6 mice were crossed to OT-I mice to generate OT-I/Kaede reporter mice (Tomura et al., 2008). Adult male and female adult mice ranging from 10-32 weeks of age were used in experiments. All mice were housed under standard conditions in animal facilities and used in accordance with the Institutional Animal Care and Use Committees guidelines at the University of Minnesota.

METHOD DETAILS

Infections

P14 immune chimeras were generated by transferring 5 X 10^{4} P14-GFP CD8 T cells into naive B6 mice intravenously (i.v.) followed by infection with 2 X 10^{5} plaque-forming units (PFU) LCMV Armstrong via intraperitoneal (i.p.) injection one day later. For CD103−/− experiments, 2.5 X 10^{4} P14-GFP CD8 T cells and 2.5 X 10^{4} P14-CFP CD8 CD103−/− T cells were co-transferred to naive B6 mice i.v. and infected with LCMV-Armstrong i.p. one day later. For OT-I and OT-I/Kaede immune chimeras, 5 X 10^{5} naive OT-I Kaede cells were adoptively transferred to B6 mice i.v. One day later, mice were infected with 1 X 10^{6} PFU of VSV- OVA i.v.

For experiments evaluating the impact of bystander inflammation on memory CD8 T cell responses, 5 X 10^{4} P14-GFP CD8 T cells were transferred into B6 mice, which were infected the next day with LCMV. At least 30 days later, these same mice received 5 X 10^{5} naive OT-I-CFP CD8 T cells i.v. and were infected orally with 1 X 10^{8} Yptb-OVA CFU (provided by Dr. Tessa Bergsbaken, Rutgers University) 1 day later (Bergsbaken et al., 2017). For experiments with LPS, 4mg/kg of LPS was i.p. injected into P14-GFP memory mice. 4-5 hours after injection, tissue was harvested for imaging. In studies evaluating self-specific responses, 5 X 10^{5} naive OT-I-GFP CD8 T cells were transferred to iFABP-OVA mice. iFABP-OVA mice were not exposed to any infectious agents.

Parabiotic surgery

Parabiotic surgery was performed as previously described (Schenkel et al., 2013). Briefly, each mouse to be paired was shaved along the opposite lateral flank. The skin was sterilized and an incision was made on the lateral aspect of each mouse. The lateral skin

incisions were conjoined using surgical wound clips. Parabionts were rested for 14–30 days before experiments. Equilibration was confirmed in the peripheral blood prior to the experimental endpoint.

Photoconversion of OT-I/Kaede CD8 T cells

Mice were anesthetized with i.p. injection of Avertin (2,2,2-Tribromalethanol) (250mg/kg). The upper abdominal area of the anesthetized mice was shaved and cleaned with Povidone iodine solution followed by 70% alcohol and a 1-2cm long, horizontal midline incision was made to expose the peritoneum. The intestine was visualized by gently retracting the skin and then a second 1-1.5cm incision was made to open the peritoneal cavity. A small loop (1cm^2) of the ileum was carefully pulled through the opening in the peritoneal cavity. Three separate spots in the tissue (~2mm^2) were exposed to a 405nm violet light at 100mW/cm^2 power for 3min/spot. The loop of intestine was returned to the peritoneal cavity and the peritoneal wall was closed with monofilament synthetic absorbable surgical suture. The skin was closed with 3-4 wound clips. Extreme care was taken to avoid activating Peyer's patches and mesenteric lymph nodes. Tissue was harvested 1 or 7 days post conversion.

Tissue harvesting and processing

Organs were harvested and digested as previously described (Thompson et al., 2016). For isolation of SI IEL, Peyer's patches were removed, the SI was cut longitudinally and then laterally into small pieces. Pieces were incubated for 30 minutes with stirring at 37°C with 0.154mg/mL dithioerythritol (Sigma-Aldrich, St. Louis, MO) in 10% HBSS/HEPES. The pieces were vortexed on high speed to dislodge intraepithelial lymphocytes and the supernatant was collected. The SI pieces were washed in RPMI containing 5% FBS and put in RPMI 1640 containing 5% FBS, 2 mM $MgCl_2$, 2 mM $CaCl_2$ and 0.5mg/mL 100 U/mL type I collagenase (Worthington, Lakewood, NJ) and incubated for 45 minutes at 37°C with stirring to obtain LPL. After enzymatic digestion, the remaining tissue pieces were mechanically disrupted using a gentleMACs dissociator (Miltenyi Biotec, San Diego, CA). Single cell suspensions from supernatant of the digestions were further separated using a 44%/67% Percoll (GE Healthcare Life Sciences, Pittsburgh, PA) density gradient. Spleen and lymph nodes (LN) were dissociated mechanically. Splenocytes and blood were treated with ACK lysis buffer to lyse red blood cells.

Tissue freezing, immunofluorescence and microscopy

Harvested murine tissues were fixed in 2% paraformaldehyde for 2 hr before being treated with 30% sucrose overnight for cryoprotection. Sucrose treated tissue was embedded in tissue freezing medium OCT and frozen in an isopentane liquid bath. Frozen blocks were processed, stained, and imaged. Stains included antibodies targeting the following markers: E-cadherin (DECMA-1, Abcam), collagen IV polyclonal antibody (Millipore), CD31 (MEC13.3, BD Horizon, San Jose, CA). Bovine α-goat (polyclonal) was used as a secondary antibody (Jackson Immunoresearch, West Grove, PA).

Flow cytometry and peptide stimulation

Isolated lymphocytes were surface or intracellularly stained with antibodies indicated in the Key Resources Table. Peptide stimulation was performed as previously described (Beura et al., 2015). Briefly, lymphocytes were plated in RPMI 1640 containing 10% FBS, 1x NEAA, 2mM L-glutamine, 1mM sodium pyruvate, 1x penicillin/streptomycin and 0.05mM β-mercaptoethanol and incubated with 1 μg/mL SIINFEKL peptide for four hours at 37°C. All samples also contained 1 μg/mL GolgiPlug (BD Biosciences, San Jose, CA). Cells were washed and stained with surface and intracellular antibodies. For intracellular stains, the BD Biosciences intracellular kit for cytokine staining was used in accordance with manufacturer's instructions. Ghost Dye™ Red 780 (Tonbo Biosciences, San Diego, CA) was used during surface staining to evaluate cell viability. Stained samples were acquired using LSRII or LSR Fortessa flow cytometers (BD Biosciences) and analyzed with FlowJo software (Treestar).

Two-photon laser scanning microscopy and analysis

Microscopy procedure

A piece of apical jejunum was harvested into warm RPMI 1640 containing 5% FBS, cut longitudinally, and mounted on a coverslip. For experiments with Hoechst stain (Invitrogen), mice were injected i.v. with 1mg of Hoechst stain 30 minutes to 24 hours before imaging. For intravital experiments, mice were anesthetized with 2%–5% isoflurane continuously inhaled via nose cone. The mouse abdomen was scrubbed with 70% ethanol and a 1-2cm horizontal midline incision was made to expose the peritoneum. A second 1-2cm incision was made to open up the peritoneal cavity and a small loop of the intestine was pulled out of the peritoneal cavity. This loop was carefully placed between two coverslips, part of a custom made apparatus designed to minimize intestinal contraction during imaging while creating a physiological and comfortable environment for the mouse (McDole et al., 2012). The mouse's normal body temperature was maintained during imaging and continuous oxygenated DMEM high glucose media lacking phenol red (Hyclone) was exchanged over the exposed piece of tissue. Rhodamine B isothiocyanate-dextran (Sigma) was injected i.v. prior to intravital imaging to assess blood flow and the health of the tissue. Movies were acquired using a MP SP5 two-photon microscope TCS (Leica) equipped with a Mai Tai HP DeepSee lasers (SpectraPhysics), an 8,000-Hz resonant scanner, a 25 × /0.95 NA objective, two non-descanned detector and two hybrid detectors.

During imaging, continuous oxygenated DMEM high glucose media lacking phenol red (Hyclone) was exchanged in the chamber containing the sample. Tissue was excited at 860 or 890nm and multiple fluorophores were imaged using the custom dichroic mirrors

with the following collections: SHG < 440nm, CFP 435-485nm, GFP 500-520nm, Hoescht 461nm. Data were processed with Imaris software (version 7.6.4 and version 8.0.1). Migrational analysis were performed using motility lab (created by the MotilityLab team, 2015: Johannes Textor, Jeffrey Berry, Mark J. Miller) or a macro (Fife et al., 2009). The drift correct function in Imaris and motility lab was used to correct SI contraction during imaging where necessary.

For each individual animal, we collected movies of at least two different locations within the jejunum separated by at least 1 mm. Within each of these macroscopic locations, we imaged 3-4 positions concurrently. We removed positions that experienced macro vibrations/contractions and are usually left with ~3-6 unique positions/animal per a given treatment condition. These individual positions were separately analyzed and averaged to identify typical cell behavior. This was repeated for several mice per condition. For presentation in figures, we showed data from one mouse that most closely approximates the typical cell behavior observed across all mice. Each dot in the motility measurement graphs represents one cell. In the legend, the "n" indicates the number of mice. It can be common for rejection to occur when transferring T cells producing novel fluorochromes (or other Ags) to new hosts for imaging or any other type of analysis for any investigator. We saw no cell behavioral differences between mice with increased attrition of T cells at memory time points (presumably due to rejection) and mice with normal memory T cell frequencies. In any case, T cells undergoing active rejection/death will be difficult to capture in the process and would likely not be imaged. If expected memory P14 T cell numbers were not detected in blood before analyzing experimental mice, we assumed rejection of memory P14 was occurring and did not use these mice for any analysis, including imaging.

Blocking with antibodies

For K^b-SIINFEKL blocking experiments, mice were i.v. injected with 100 μg of anti-K^b-SIINFEKL antibody 1-2 hr before imaging (25-D1.15, BioXcell). An irrelevant IgG1 antibody was used as an isotype control under the same conditions (MOPC-21, BioXcell).

Mathematical modeling of TPLSM data

For calculating volume, a 360 μm by 360 μm by 360 μm domain was divided into 2.5 μm x 2.5 μm x 2.5 μm cubes. There were 2,985,984 = $(360/2.5)^3$ such cubes. Each cell was initially translated so that its minimum in the x-, y-, and z-directions coincided with the origin (0,0,0). As the cell moved through the domain using observed positions, the distance between the cell and each of the cubes was calculated. An algorithm was used to compute these distances. If the distance between the cell and a cube center was less than a radius of a cell (assumed to be 5 μm), then cube volume was counted as part of the total volume traversed by the cell. A specific cube volume is only counted once. The total volume traversed by the cell (μm^3) is divided by the time the cell was observed (in seconds). Straightness analysis was performed as previously described (Mrass et al., 2017). Briefly, for every experimental track, 100 track-derivatives were generated, by randomizing the orientation of individual velocity vectors. The magnitude of the velocity vectors was left unchanged and therefore the average speed was identical in experimental and randomized tracks. The displacement between the start and end of the experimental track and the displacements of 100 randomized tracks were used to calculate the straightness *Z*-score. It shows how many standard deviations the experimental displacement deviates from the expected displacement of all randomized track derivatives. Negative Z-scores suggest that the experimental displacement is less than expected by chance ("confined tracks") and positive *Z*-scores suggest that the experimental displacement is higher than expected by chance ("straight tracks").

For modeling the length of time expected for P14 CD8 T cells to scan a villus, frequency distributions were created for speed and turning angles using day 30 T cell data within the villi. Simulations were performed using a cylinder with a diameter of 75 μm and a height of 300 μm, to mimic the shape and size of a single villus in the jejunum. A simulation was performed with 60 cells uniformly distributed within the cylinder (Figure 2A) and with one T cell initially positioned at the center of the cylinder (Figure S2A). T cells sample from the speed and turning angle distributions each time step to advance their position in time. The turning angle determined a cone on which the T cell remained when advancing its position. A time step of 20 s was used for the simulation of 60 cells, and a time step of 60 s was used for one cell. The cylinder was divided into 85,789 2.5 μm by 2.5 μm by 2.5 μm cubes. A cube was counted toward the total volume patrolled if the distance between a cube center and any T cell was less or equal to the T cell radius (3.5 μm). A cube that had been surveyed remained permanently surveyed for the duration of the simulation. If a T cell attempted to exit the cylinder, it was assigned its previous position with a random 0.5 μm displacement component in the x-, y-, and z-direction, such that it remained within the cylinder. The simulations with 60 cells and one cell were repeated 100 times to create error bars. Error bars plot the maximum and minimum volume patrolled over the 100 simulations at a specific time.

QUANTIFICATION AND STATISTICAL ANALYSIS

D'Agostino and Pearson test was performed to evaluate normality. A Mann-Whitney test was performed when two unpaired groups being compared did not exhibit Gaussian distribution. When a single variable between multiple groups with normal distribution was compared, a one-way ANOVA with Dunn's multiple comparison was employed. For single variable comparisons across multiple groups of non-Gaussian distribution, a Kruskal-Wallis test was used. All statistics were performed using Prism (GraphPad Software, V7) and for all analysis *p* values of less than 0.05 were considered significant, as indicated by one or more asterisks (*).